Acta Pharmaceutica Sinica B 2022;12(3):1432−1446

Chinese Pharmaceutical Association
Institute of Materia Medica, Chinese Academy of Medical Sciences

Acta Pharmaceutica Sinica B

www.elsevier.com/locate/apsb
www.sciencedirect.com

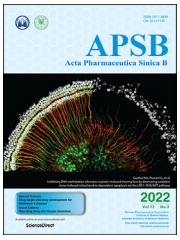

ORIGINAL ARTICLE

Chiral mesoporous silica nano-screws as an efficient biomimetic oral drug delivery platform through multiple topological mechanisms

Yumei Wang[a], Jia Ke[a], Xianmou Guo[a], Kaijun Gou[a], Zhentao Sang[b], Yanbu Wang[a,b], Yan Bian[b], Sanming Li[a,*], Heran Li[b,*]

[a]*Department of Pharmaceutics, Shenyang Pharmaceutical University, Shenyang 110016, China*
[b]*School of Pharmacy, China Medical University, Shenyang 110122, China*

Received 7 June 2021; received in revised form 8 July 2021; accepted 4 August 2021

KEY WORDS

Chiral mesoporous silica;
Nano-screw;
Morphology;
Geometric topological structure;
Intestinal epithelium barrier;
Oral adsorption

Abstract In the microscale, bacteria with helical body shapes have been reported to yield advantages in many bio-processes. In the human society, there are also wisdoms in knowing how to recognize and make use of helical shapes with multi-functionality. Herein, we designed atypical chiral mesoporous silica nano-screws (CMSWs) with ideal topological structures (*e.g.*, small section area, relative rough surface, screw-like body with three-dimension chirality) and demonstrated that CMSWs displayed enhanced bio-adhesion, mucus-penetration and cellular uptake (contributed by the macropinocytosis and caveolae-mediated endocytosis pathways) abilities compared to the chiral mesoporous silica nanospheres (CMSSs) and chiral mesoporous silica nanorods (CMSRs), achieving extended retention duration in the gastrointestinal (GI) tract and superior adsorption in the blood circulation (up to 2.61- and 5.65-times in AUC). After doxorubicin (DOX) loading into CMSs, DOX@CMSWs exhibited controlled drug release manners with pH responsiveness *in vitro*. Orally administered DOX@CMSWs could efficiently overcome the intestinal epithelium barrier (IEB), and resulted in satisfactory oral bioavailability of DOX (up to 348%).

Abbreviations: APTES, 3-aminopropyltriethoxysilane; $AUC_{0-\infty}$, area under the curve; AR, aspect ratio; C_{max}, maximum concentration; CMSs, chiral mesoporous silicas nanoparticles; CMSWs, chiral mesoporous silica nano-screws; CMSRs, chiral mesoporous silica nanorods; CMSSs, chiral mesoporous silica nanospheres; C_d, drug loading capacity; DAPI, 4,6-diamidino-2-phenylindole; DOX, doxorubicin; DCM, dichloromethane; EDC·HCl, 1-(3-dimethylaminopropyl)-3-ethylcarbodiimide hydrochloride; FBS, fetal bovine serum; FITC, Fluorescein isothiocyanate; F_{rel}, relative bioavailability; TEOS, ethylsilicate; GI, gastrointestinal; HOBT, 1-hydroxybenzotriazole; IEB, intestinal epithelium barrier; IR, infrared spectroscopy; Mβ-CD, methyl-β-cyclodextrin; $MRT_{0-\infty}$, mean residence time; MSNs, mesoporous silica nanoparticles; NPs, nanoparticles; nano-DDS, nano-drug delivery systems; *N*-PLA, *N*-palmitoyl-L-alanine; PBS, phosphate buffer solution; RBCs, red blood cells; RITC, rhodamine B isothiocyanate; SARS-CoV-2, severe acute respiratory syndrome coronavirus 2; SBF, simulated body fluid; S_{BET}, Specific surface area; SD, Sprague−Dawley; SGF, simulated gastric fluid; SIF, simulated intestinal fluid; $t_{1/2}$, half-life; T_{max}, peak time; V_t, pore volume; W_{BJH}, pore diameter; XRD, X-ray diffractometry.

*Corresponding authors.
E-mail addresses: li_sanming@126.com (Sanming Li), liheranmm@163.com (Heran Li).

Peer review under responsibility of Chinese Pharmaceutical Association and Institute of Materia Medica, Chinese Academy of Medical Sciences.

https://doi.org/10.1016/j.apsb.2021.08.014

CMSWs were also proved to exhibit good biocompatibility and unique biodegradability. These findings displayed superior ability of CMSWs in crossing IEB through multiple topological mechanisms and would provide useful information on the rational design of nano-drug delivery systems.

1. Introduction

Oral administration is recognized as the most convenient drug delivery route because of its noninvasion and best patient-based compliance[1−5]. Nevertheless, there are huge challenges for the oral delivery of a majority of drugs due to the complex physiological/chemical barriers in gastrointestinal (GI) tract [*e.g.*, gastric pH condition, GI enzymatic degradation, and intestinal epithelium barrier (IEB)], which protect the internal tissues and organs from invasion of harmful agents, contribute to the homeostasis of microenvironment, and meanwhile limit the effective absorption of various therapeutic molecules[6−8]. Among these intestinal barriers, IEB (including the mucus layer and epithelial cells) is considered to be the major barrier to prevent intact nanoparticles (NPs) from efficiently entering the blood circulation through oral administration[6,9]. Although the delivery efficacy can be greatly improved with the assistance of nano-drug delivery systems (nano-DDS) existing smart stimulus-triggered drug release performance, the low-efficiency oral absorption property of current nano-DDS still greatly restricts their biomedical applications. One of the main reasons is that, the vast majority of nano-DDS are spherical in the current clinical trials or lab-scale studies due to their ease of synthesis, which can minimize the surface free energy, and maintain the hydrostatic equilibrium. They also exhibit some mechanical properties, such as strong stability, good flowability, and impact resistant ability. However, from a geometric perspective, spheres always mean large section area, small contact area ("point" contact) and smooth surface, which are disadvantage for many bio-processes and greatly limit the effectiveness of such drug delivery systems. Along with the advance of self-assembly strategies and the deeper understanding on the growth of NPs, non-spherical nanomaterials, such as rod-shaped, hollow rod-shaped, dendrimer-like, virus-like and core−shell structures, have been gradually synthesized in recent years. Yu et al.[10] revealed that rod-shaped NPs showed faster diffusion than their spherical counterparts in the mucus layer due to the rotation-facilitated mechanism, and thus contributing to a better mucus permeability and a longer GI detention time. This finding informs us that the shape of NPs may influence the biological effects, and non-spherical shapes may be a better choice though currently conventional spherical NPs remain the dominant one.

Faced with such an adversity, we began to gain inspirations from the microorganisms with superior adaptability and functionality in the GI tract. One of the first things we learn in microorganisms is that they come in a wide variety of shapes in nature: from spherical HIV viruses to rod-like *Tobacco mosaic* viruses and *Escherichia coli* bacterias[11,12], and even the current epidemic corona-liked severe acute respiratory syndrome coronavirus 2 (SARS-CoV-2) viruses. Morphology diversity not only endows superiorities to the evolution and development of creatures, but also is always consistent with functions as a result of biological evolution. For example, some viruses with spike protein rough surface present excellent cellular invasion through strongly binding to bio-membranes[13]. Likewise, the rod-shaped microbes having small section area have been reported to swim through the intestinal mucus and remain in the mucus layer for extended periods, and are beneficial for the absorption in the GI tract[10,14,15]. Among the microorganisms, helical bacteria, such as campylobacter jejuni (the bacteria that causes bacterial-induced diarrhea) and *Helicobacter pylori* (which induce stomach ulcers), are a kind of bacteria with helical body shapes[16,17]. They possess strongly pathogenicity *in vivo*, and have been reported to yield some advantage in many bio-processes, including penetration, adhesion, colonization and invasion. In both cases (*Campylobacter jejuni* and *H. pylori*), the loss of the helical shape (which can be destroyed by fairly simple gene knockouts) can result in a reduction on colonization and virulence, and the ability of the bacteria to function within the body. Particularly, helical *C. pylori* have been discovered to infect the human stomach through the strong adhesion on the gastric mucosa and the gastric intercellular space. Moreover, it has been reported that helical campylobacter pylori can swim more than 15% faster than their isogenic rod-shaped mutants. It seems that the geometric topological structure of microorganisms is close associated with their bio-functionality on the microscale. In the human society, there are also wisdoms in knowing how to recognize and make use of helical shapes. Tools with special helical shapes (*e.g.*, screw-spike, corkscrew, screw-wedges and propellers) are designed and endowed with incredibly functionality, such as strong fastening, high penetration, effort-saving, and alteration of the magnitude or direction (or both) of an applied force. Inspired by the above-mentioned aspects, we designed inner and outer dual-helical nano-screws (named as CMSWs) with long and twist body, relative rough surface, and three-dimension chiral topological structure. We hypothesized that the ideal engineered nano-screws could penetrate the IEB more efficiently than nanospheres and nanorods.

With the development of nanomedicine, mesoporous silica nanoparticles (MSNs) with a pore size range of 2−50 nm are regarded as one of the most promising nano-DDS of various therapeutic molecules owing to their prominent features (*e.g.*, relative rigid structure, large surface area and pore volume, controllable particle size and pore size, diverse morphology, ease modified surface, and intrinsic biocompatibility)[18]. In this study, chiral mesoporous silicas nanoparticles (CMSs) with different morphologies (including spherical CMSSs, rod-shaped CMSRs and screw-liked CMSWs) were fabricated by varying the ratios of reactants. The structural and physicochemical properties of CMSs were systemically characterized. To explore how the topological structures of CMSs influence on the oral adsorption process, bio-adhesion, mucus-penetrating properties, uptake cellular efficiency and mechanisms, the GI tract retention ability, and the plasma concentration of CMSs were evaluated. Furthermore, doxorubicin (DOX) was selected as the model drug and was loaded into CMSs to experimentally evaluate their drug delivery functions. After a

detailed exam of the drug loading ability, *in vitro* release experiments were carried out in phosphate buffer solution (PBS) with varied pH values. Moreover, DOX retention and absorption in rat small intestine were evaluated. *In vivo* pharmacokinetic study was also conducted to certificate the biological behavior advantageous of CMSWs. Finally, the biodegradability of CMSs and the *in vitro*/*in vivo* biocompatibility of CMSWs were studied. We believe that the CMSWs with potential topological advantages are a promising oral drug delivery platform owing to their superior biological responses and controllable release behavior.

2. Materials and methods

2.1. Materials and chemical reagents

1-(3-Dimethylaminopropyl)-3-ethylcarbodiimide hydrochloride (EDC·HCl) and 1-hydroxybenzotriazole (HOBT) were obtained from GL Biochem Ltd. (Shanghai, China). *N*,*N*-Dimethylformamide (DMF) and dichloromethane (DCM) were purchased from Shanghai Jinjinle Industrial Co., Ltd. L-Alanine methyl ester hydrochloride (H-s-Ala-Ome·HCl), ethylsilicate (TEOS), 3-aminopropyltriethoxysilane (APTES), palmitic acid and doxorubicin hydrochloride (DOX) were purchased from Aladdin (Shanghai, China). Fluorescein isothiocyanate (FITC), rhodamine B isothiocyanate (RITC) and 4,6-diamidino-2-phenylindole (DAPI) were purchased from Beijing Bailingwei Technology Co., Ltd. (Beijing, China). Double distilled water was obtained by ion exchange and used in all experiments.

Caco-2 cells were purchased from the American Type Culture Collection (ATCC, China), and were cultured in Dulbecco's modified Eagle's medium (DMEM; Gibco, Carlsbad, CA, USA) supplemented with 10% (*v*/*v*) fetal bovine serum (FBS; HyClone, Conroe, TX, USA), 1% (*v*/*v*) L-glutamine, 1% (*v*/*v*) non-essential amino acid and 1% penicillin and streptomycin (100 IU/mL) at 37 °C in 5% CO_2.

Animals were purchase from the animal standard Laboratory center and approved by the Committee on the Ethics of Animal Experiment of Shenyang Pharmaceutical University (Shenyang, China). All animals received care in accordance with the guidelines for the Committee on the Ethics Animals.

2.2. Preparation of CMSs with different morphologies

The anionic surfactant templates of *N*-palmitoyl-L-alanine (*N*-PLA) were synthesized using a previously reported method[19]. The multiple CMSs with different morphologies were prepared according to the previous method with some modification[20–22]. For the fabrication of CMSSs, 1.1 mmol N-PLA was dissolved in 10 mL deionized water and 10 mL NaOH (0.1 mol/L) on 35 °C water bath. Until completely dissolve, 2 mL HCl (0.01 mol/L) was added under stirring for 1 h. Afterwards, a mixture of 0.24 mL APTES (0.227 g, 1 mmol) and 1.57 mL TEOS (1.458 g, 7 mmol) was dropped into the above solution with the stirring rate of 600 rpm by ZNCL-S-10D magnetic stirrer (Gongyi, China) at room temperature for 10 min. Then the system was remained statically for 24 h, centrifuged, water and ethanol alternately washed and dried. Finally, the dried sample was produced by extraction method with an ethanolamine ethanolic solution of (17%, *v*/*v*) for 24 h at its boiling temperature.

Additionally, for the synthesis of CMSRs, 1 mmol N-PLA was dissolved in 22.7 mL deionized water and 8.6 mL NaOH (0.1 mol/L) with stirring at 35 °C water bath. Afterwards, 1.4 mL HCl (0.1 mol/L) was added to the above dissolved solution under vigorous stirring to partially acidify the salt. After the mixture was stirred for 1 h, a mixture of 1.5 mL TEOS (1.4 g, 6.72 mmol) and 0.091 mL APTES (0.086 g, 0.39 mmol) was added to the above mixture with stirring rate of 600 rpm at room temperature for 10 min followed by statical placement for 2 h. The mixture was finally cured at 80 °C for additional 15 h. The solid product was recovered by centrifugal separation, water and ethanol alternately washed and dried at 80 °C. The anionic surfactants were removed by reflux with an ethanolamine ethanolic solution of (17%, *v*/*v*) for 24 h at its boiling temperature.

To improve the morphology of CMSRs, we optimized the synthesis method and obtained CMSWs. In a typical synthesis, the following steps were repeated: a mixture of 1.5 mL TEOS (1.4 g, 6.72 mmol) and 0.091 mL APTES (0.086 g, 0.39 mmol) was added to the mixture with stirring rate of 600 rpm at room temperature for 10 min followed by statical placement for 2 h. Other steps were consistent with the synthesis process of CMSRs.

For the synthesis of FITC-CMSs, FITC was firstly linked with APTES in ethanol by covalent bond, and then 20 mg of engineered CMSs were added to form the conjugation. The reaction was remained for 8 h with vigorous stirring at room temperature, and then centrifuged, washed with ethanol, and ultrasonicated several times until the unconjugated FITC and APTES was completely removed.

2.3. Characterization

The morphologies of the prepared CMSs were studied by a TEM instrument (FEI Tecnai G2-F30) and a SEM instrument (JEOL JSM-6510 A), respectively. Hydrodynamic diameters and Zeta potential of CMSs were detected by Malvern Zetasizer NanoZS90 based on the dynamic light scattering tests. N_2 adsorption−desorption isotherms and pore size distributions were obtained at 77 K using a V-Sorb 2800P equipment. The structure information and the interaction between drug and carriers were confirmed by infrared spectroscopy (IR) with wavenumber range from 400 to 4000 cm^{-1}. Samples were carefully grinded and mixed with dried KBr in a mortar and pestle to obtain KBr disks. X-ray diffractometry (XRD) measurements were performed on DX-2700 diffractometer at 30 mA and 30 kV equipped with a Ni-filtered Cu-Ka radiation in a 2θ range of 5−40° using a step size of 0.02°. The physical state (*i.e.*, melting point) was characterized by differential scanning calorimetry (DSC) 2500 instrument at a heating rate of 10 °C/min with the temperature from 25 to 300 °C. Small X-ray scattering (SAXS) patterns were collected from SAXSpace operated at 40 kV and 50 mA with a Ni filtered Cu-Ka radiation. The surface wettability can evaluate through contact angle measurement using the static drop technique. Water contact angles were measured on JCY-1 contact angle tester by using contact mode (the images were recorded every 5 s for all the samples). Before measurement, 50 mg of the powder sample was pressed into flakes under the pressure of 4 MPa using FW-4A tablet machine.

2.4. Bio-retention ability

The bio-adhesion study of CMSs was carried out according to the previous elution method with some modification[23]. To be specific, Sprague−Dawley (SD) rats (200±20 g) were fasted overnight with free access to water and sacrificed to separate small intestine

tissues. After carefully washed with normal saline (keeping the mucus layer intact), the small intestine tissues were cut into 1 cm × 4 cm segments, and spread on the glass slide with an angle of 45° to the glass funnel. Afterwards, the prepared CMSs (10 mg) were respectively and evenly spread on the above prepared small intestine tissues. After that, CMSs were eluted from the isolated small intestine tissues using simulated intestinal fluid (SIF) at a flow rate of 2 mL/min for 1, 2, 3, 4, and 5 min (a schematic diagram of the apparatus was shown in Supporting Information Fig. S1). Finally, the effluent was centrifuged and dried at 60 °C. The bio-adhesion capacity of CMSs was quantitatively evaluated by weight loss method in triplicate and the bio-adhesion ratio was calculated according to Eq. (1):

$$\text{Bio-adhesion}(\%) = \frac{W_0 - W_e}{W_0} \times 100 \quad (1)$$

where W_0 is the initial weight of the CMSs samples, and W_e is the weight of the collected effluent.

In addition, the bio-adhesion capacity of FITC-CMSs was qualitatively accessed by *ex vivo* imaging technology. To be specific, the FITC-CMSs were spread on the small intestine tissues (1 cm × 4 cm) and eluted using SIF medium at a flow rate of 2 mL/min for 5 min. After that, the fluorescence images of FITC-CMSSs, FITC-CMSRs and FITC-CMSWs were recorded by a Carestream FX PRO (Bruker/Carestream, Inc., USA) equipped with an excitation filter of 470 nm and an emission filter of 535 nm. The average fluorescence intensity accumulated in the small intestine tissues were quantitatively evaluated by a region-of-interest (ROI) analysis on the FITC signal intensity.

2.5. Mucoadhesion and mucus permeation properties

FITC-CMSs (1 mg/mL) were cultured with 3 mL simulated gastric fluid (SGF) and SIF at 37 °C, respectively. At the predesigned points, 0.2 mL FITC-CMSs suspension were drawn out and analyzed using microplate reader (Bio-Rad Laboratories Ltd., Hertfordshire, UK) to record the fluorescence spectra in the wavelength range of 475−700 nm using scan step of 10 nm. After the reaction completed, the supernatant was collected by centrifugal separation of FITC-CMSs and the fluorescence spectra of supernatant were record to investigate the fluorescence stability of FITC-CMSs at SGF an SIF medium.

For exploring the three-dimensional penetration ability of NPs, the isolated small intestinal was obtained. Firstly, the isolated small intestine was cut into 2.5 cm segments. After staining the intestinal segments with 500 μL RITC solution (10 μg/mL) for 10 min, 100 μL PBS solution containing FITC-labeled NPs (100 μg/mL) was slowly injected. The intestinal loops were ligated and incubated in Krebs–Henseleit (KH) buffer at 37 °C. After 30 min, intestinal loops were washed with physiological saline to remove the free NPs and then was cut along the midline. The intestinal segments were spread out in a living cell culture dish (intestinal cavity side downward) without fixation and 3D images were obtained by confocal laser scanning microscopy (CLSM, Nikon C2 Confocal, Tokyo, Japan) scanning in Z-stack mode immediately.

Moreover, the fresh mucus (200 μL) was carefully isolated from the lumen side of small intestinal and incubated with FITC-CMSs samples (200 μg/mL in PBS, 10 μL) at 37 °C for 30 min, respectively. Immediately, videos (frame rate: 37 fps, 2 s and 10 s) of the motion trajectories of different CMSs in mucus solutions were captured by inverted fluorescence microscope (DMI4000B, Leica, Germany) and were analyzed using ImageJ software, which is well-known as the multiple particle tracking method[10].

2.6. Cellular uptake

Caco-2 cells in logarithmic growth phase were seeded in 24-well plates at a density of 5×10^4 cells/well, in which 1.0 mL of complete medium was added and placed in a 37 °C incubator for 48 h with 5% CO_2. When the cells grew to 80%−90% in the pore plates, the culture medium was discarded and replaced with 1.0 mL of CMSs samples (0.25 mg/mL) labeled with FITC, respectively. After an incubation at 37 °C for 4 h, the cells were washed three times with cold PBS, fixed with 4% formaldehyde and stained by 0.2 mL DAPI (5 μg/mL) for 15 min. Afterwards, cells were washed twice with PBS in ice bath and sealed the climbing tablets with 90% glycerin solution. Finally, CLSM was applied to qualitatively observe the uptake behavior of three types of engineered NPs.

2.7. Cellular uptake mechanisms

In order to study the cellular uptake mechanisms, three specific inhibitors were introduced to investigate the endocytic pathways of CMSs. In this study, cells were first incubated in PBS with or without specific inhibitors for 30 min at 37 °C and subsequently exposed to 1.0 mL of CMSs (0.25 mg/mL) labeled with FITC for 1 h at 37 °C, in which a blank control group was performed in PBS without inhibitors for CMSs. Additionally, when methyl-β-cyclodextrin (Mβ-CD, 1 μg/mL) was present to delete cholesterol from the cell membrane, further to inhibit caveolae-mediated endocytosis. Cytochalasin D (5 μg/mL) was used to inhibit the endocytosis pathway of micropinocytosis[24]. The inhibition of clathrin-mediated endocytosis was achieved by chlorpromazine inhibitor (10 μg/mL).

2.8. Retention in the GI tract

The GI tract retention ability of CMSs, DOX and DOX@CMSs after oral administration was investigated *via ex vivo* imaging technology. For CMSs, they were labeled with FITC for *ex vivo* tracking before the experiment. 54 SPF-grade male Kunming mice (20±2 g) were fasted overnight with free access to water and then were randomly divided into 3 groups (n=18 per group, n=3 at each time point). These 3 groups were orally administrated with 0.5 mL FITC-CMSSs, FITC-CMSRs and FITC-CMSWs normal saline suspensions (4 mg/mL), respectively. For DOX and DOX@CMSs samples, 24 SPF-grade male Kunming mice (20±2 g) were randomly divided into four groups and orally administrated with 0.5 mL DOX, DOX@CMSSs, DOX@CMSRs and DOX@CMSWs (the dose equal to 10 mg/kg of DOX) normal saline solutions, respectively. At predesigned intervals, animals were sacrificed, and the entire GI tract (including stomach and small intestine) were excised. The fluorescence images of FITC-CMSs, DOX and DOX@CMSs samples were recorded by a Carestream FX PRO (λ_{ex}=470 nm, λ_{em}=535). The CMSs samples accumulated in the stomach and small intestine were quantitatively evaluated by a ROI analysis on the FITC signal intensity.

2.9. In vivo blood circulation of CMSs

To study the *in vivo* blood circulation of CMSs, 12 healthy Kunming mice (30±2 g) were randomly allocated into four groups

($n=3$): control group, CMSSs group, CMSRs group and CMSWs group, which were intragastrically administrated with normal saline or CMSs suspensions (at a dose of 60 mg/kg) using a lavage needle, respectively. At predesigned intervals, supraorbital venous blood (~0.15 mL) was collected into tubes containing heparin and stored at 4 °C. After blood collection at all scheduled time points, the plasma was separated from the whole blood by centrifugation at 4000 rpm for 5 min. Subsequently, Si contents of plasma samples were detected by ICP-MS using the calibration curve.

2.10. Drug loading and release

Drug loading were performed by organic solvent drying method. Briefly, 2 mg DOX was precisely weighted and sufficiently dissolved in 2 mL absolute alcohol to get a high-concentration drug solution (1 mg/mL). Afterwards, the above solution was mixed with 8 mg CMSs under mild stirring for 24 h at room temperature. After being dried under environment condition, the mixture was washed with pH 7.4 PBS solution and centrifuged until the supernatant was transparent. The drug loading efficiency was measured by ultrasonic extraction of DOX from absolute alcohol solution and then the content of drug was determined by ultraviolet spectroscopy (UV-1750, Shimadzu, Japan) at the wavelength of 480 nm. The loading capacity (C_d, %) were calculated based on Eq. (2):

$$C_d(\%) = \frac{W_2}{W_1} \times 100 \quad (2)$$

where W_2 is the weight of DOX in CMSs, and W_1 is the weight of CMSs.

The drug release of DOX and DOX@CMSs were determined by dialysis method *in vitro*. The process of drug release was designed as follows: 100 μg DOX and DOX@CMSs with equivalent of 100 μg DOX were separately mixed with 1 mL PBS and then added into the dialysis bag with molecular weight cutoff of 3500 Da. Then the prepared dialysis bags were placed in 9 mL PBS solution with different pH values for 100 rpm at 37 °C. At specified intervals, 0.2 mL the sample solution was drawn out to place into 96-well plates and immediately replenished by the same volume of release medium. The fluorescence intensity ($\lambda_{ex}=480$ nm; $\lambda_{em}=580$ nm) of DOX was analyzed using microplate reader. The cumulative release (Cr, %) was quantitatively calculated according to Eq. (3):

$$\text{Cr } (\%) = \frac{W_t}{W_{\text{total}}} \times 100 \quad (3)$$

where W_t indicates the amount of drug released at predesigned time (t) and W_{total} is the initial amount of drug loaded in the CMSs.

2.11. Drug absorption in rat small intestine

To investigate the small intestine absorption of DOX and DOX@CMSs, four male SD rats (200±20 g) were intragastrically administered with DOX@CMSs and DOX normal saline suspensions (the dose equal to 5 mg/kg of DOX). Two hours later, rats were euthanized, and the middle small intestine segments were excised. The intestinal tissues were carefully cleaned with PBS, frozen with OCT agents immediately, sliced at a depth of 15 μm by a cryostat (Leica, Wetzlar, Germany), stained with DAPI, and detected by CLSM instrument.

2.12. In vivo pharmacokinetic

Twelve SD rats were randomized into four groups ($n=3$), and different DOX formulations (DOX@CMSSs, DOX@CMSRs and DOX@CMSWs, a dose equivalent to 30 mg/kg of DOX) and DOX (30 mg/kg) were orally administered. At predesigned intervals, approximately 0.5 mL blood samples were taken from eye venous sinus and centrifuged immediately at 4000 rpm for 5 min to obtain plasma (supernatant), and then stored the supernatants at −20 °C for further analysis. Plasma samples were treated according to the previous reference 25. The key pharmacokinetic parameters, including area under the curve ($AUC_{0-\infty}$), half-life ($t_{1/2}$), maximum concentration (C_{max}), peak time (T_{max}) and mean residence time ($MRT_{0-\infty}$) were determined using DAS.2.1 version. The relative bioavailability was calculated by the following Eq. (4):

$$F_{rel}(\%) = \frac{(AUC_{0-\infty})T/DoseT}{(AUC_{0-\infty})R/DoseR} \times 100 \quad (4)$$

where F_{rel} is the relative bioavailability, T refers to the different DOX formulations, and R refers to DOX.

2.13. In vitro biodegradation of CMSs

In vitro biodegradation property was evaluated using weight loss method. Specifically, CMSs samples were precisely weighted, sealed and immersed into SGF, SIF and simulated body fluid (SBF) at a particle concentration of 1.0 mg/mL, respectively, with a gentle shaking rate of 150 rpm at 37 °C. After 1 week, the residues were centrifuged, gently washed with deionized water, dried at 60 °C, and weighted for quantifying the biodegradation activity. The particles after degradation were characterized by TEM. The biodegradation ratio was calculated using Eq. (5):

$$\text{Degradation ratio}(\%) = \frac{W_t - W_r}{W_t} \times 100 \quad (5)$$

where W_t is the weight of added CMSs and W_r is the weight of residues.

2.14. Hemolysis assay

Hemolysis assay of red blood cells (RBCs) was carried out to explore the blood compatibility of CMSWs. Firstly, fresh blood sample was collected from eye venous sinus of SD rats, and the RBCs were isolated from serum by centrifugation, and washed three times with sterile normal saline. Then, RBCs were diluted to a concentration of 2% (v/v) solution by sterile normal saline and were separately mixed with an equal volume of CMSWs solutions at different concentrations (25, 50, 100, 200, 400 and 800 μg/mL), and the hemolytic photographs of RBCs were obtained after 0.5, 2, 4 h standing. Herein, RBC diluted with D.I. water and sterile normal saline were acted as the positive and negative controls, respectively. After standing at room temperature for 4 h, all the sample tubes were centrifuged at 8000 rpm for 5 min, the hemolytic photographs of RBCs were taken and the absorbances of the supernatants were detected using ultraviolet spectroscopy ($\lambda_{max}=541$ nm). The percent hemolysis ratio of RBCs was calculated based on the following Eq. (6):

$$\text{Hemolysis ratio}(\%) = \frac{A_{sample} - A_{\text{negative}}}{A_{\text{positive}} - A_{\text{negative}}} \times 100 \quad (6)$$

where A_{sample} represents the absorbance value of the tested group, $A_{negative}$ and $A_{positive}$ are the absorbance value of positive and negative controls, respectively.

2.15. *In vitro toxicity*

In vitro cytotoxicity of CMSWs was determined by MTT assay. Caco-2 cells were first seeded in 96-wells plates (5×10^4 cells/well) and incubated at 37 °C under 5% CO_2 for 24 h. After that, the cells were separately treated with various concentrations of CMSWs suspensions (0, 10, 20, 50, 100, 200, 300 and 400 μg/mL) for 24 h. Subsequently, the medium was removed and replaced with 10 μL MTT solution for further 4 h. Before test, the supernatant was discarded and replaced with the addition of 150 μL DMSO to dissolve crystals by gentle shaking, and the absorbance was detected using a microplate reader at 490 nm. Each experiment was repeated five times.

2.16. *In vivo toxicity*

To further explore the *in vivo* toxicity of CMSWs, the rats in CMSWs group were orally administrated with CMSWs at a dose of 60 mg/kg once a day for 14 days with saline group as a control. After administration, the body weight was recorded every other day. On Day 14, blood was drawn from ocular vein for hematology analysis. Blood biochemical assay was analyzed using a Biochemical Autoanalyzer (Type 7170, Hitachi, Japan). Afterwards, the rats were euthanized, the GI tract and the tissues (heart, liver, spleen, lung and kidney) were excised, weighted and further analyzed by H&E staining. The organ/body ratio (%) was calculated as the ratio of tissues (wet weight, mg) to body weight (g).

2.17. *Statistical analysis*

All data were expressed as mean ± standard deviation (SD). Student's *t*-test and one-way ANOVA were applied to evaluate statistical significance. A P-value < 0.05 was considered statistically significant.

3. Results and discussions

3.1. *Morphology and structure of the prepared CMSs*

To elucidate how the topological structures of NPs influence on their oral drug delivery efficiency, CMSs with various morphologies were prepared by varying the ratios of reactants *via* co-structural-directing-agent method (Fig. 1A)[20−22]. The successful synthesis of the template N-PLA and the CMSs were characterized by IR analysis (Supporting Information Fig. S2). The morphologies of CMSs were presented in the TEM and SEM images (Fig. 1B−D). To be specific, CMSSs was well-formed spherical NPs with a diameter of approximately 70 nm and an aspect ratio (AR) of 1.0. CMSRs exhibited a short rod-like morphology with a dimension of 153 nm × 259 nm and a calculated AR of 1.7. In particular, CMSWs had a long and twist screw-like body, exhibiting a dimension of 43 nm × 192 nm and an AR of 4.5. The hydrodynamic diameters of CMSSs, CMSRs and CMSWs were 78, 231 and 350 nm, respectively (Fig. 1E). The measured value is slightly larger than the actual size of CMSs on account for the hydration effect. Moreover, CMSWs had a relative rough surface with inner and outer dual-helical macroscopic chiral topological structure compared to CMSSs and CMSRs (Fig. 1B), which is beneficial for the extensive surface interaction with the biological hosts[13]. Meanwhile, CMSs were proven to have uniform mesoporous structures. As manifested in Fig. 2A, SAXS patterns of CMSRs and CMSWs showed well-resolved peaks at very scattering angles, indicating the highly ordered mesopore structure, while CMSSs exhibited inconspicuous peaks, suggesting the low pore structure order degree. As shown in Fig. 2C, N_2 adsorption−desorption isotherms of CMSs were typical type IV isotherms with clear hysteresis loops, demonstrating the existence of uniform mesoporous. The calculated parameters were listed in Table 1. The average pore size of CMSWs (3.8 nm) was slightly larger than that of the CMSRs and CMSSs (3.7 nm, Fig. 2B and Table 1). The Zeta potential of CMSSs, CMSRs, CMSWs were 9.42±0.63, 10.54±0.56 and 9.14±0.46 mV, respectively, ensuring that the three types of CMSs had the same surface charge (Fig. 2D).

3.2. *Bio-retention ability of CMSs in vitro*

It is well known that small intestine is the main place for oral adsorption. IEB, including the mucus layer and epithelial cells, acts as the main barrier for the oral administration. Broadly speaking, drug adhesion (retention) on the small intestine is the premise for effective oral delivery *in vivo*. Theoretically, it is possible to achieve a high absorption or uptake by producing a larger contact area and a longer contact time with the small intestinal tract. As above mentioned, although nanospheres exhibit some mechanical advantages, the spherical shape always means large section area and small contact area ("point" contact, as indicated in Fig. 3A). It may not be a best choice for oral delivery from a geometric perspective. Nanorods, known as NPs exhibiting smaller section surface and larger contact area ("line" contact, Fig. 3A), are beneficial for the adhesion, transport and penetration capability in IEB. Zhang et al.[14] designed and prepared rod-like MSNs with enhanced cellular uptake and higher oral bioavailability of DOX. We further designed atypical CMSWs with long and twist body and three-dimension chiral topological structure, and hypothesized that nano-screws would adhere and penetrate the IEB more efficiently than nanospheres and nanorods. Firstly, as a precondition for bio-adhesion, the wettability of CMSs was evaluated through contact angle measurement using the static drop technique. It is a significant interfacial property to assess the surface hydrophilic and hydrophobic properties of bio-materials[25,26], and is close related to the *in vivo* biological behavior of MSNs. According to Fig. 2E, the initial water contact angle values (at 5 s) of CMSSs, CMSRs and CMSWs corresponded to 44.35°, 35.17° and 27.04°, respectively, suggested good wettability. The contact angles of CMSs were gradually decreased with the increasing capture time, and both the initial and equilibrium contact angles of CMSWs were obviously lower than that of CMSSs and CMSRs (Fig. 2E and F), which was also powerful evidence on the large contact area and the rough surface of CMSWs. Meanwhile, the wettability results indicated that water could enter into the internal surface of mesoporous channel, which was beneficial for the release of the payloads. The bio-retention study was then performed *ex vivo* on small intestinal mucosa under mild downward flow elution. The bio-retention images and the bio-adhesion profiles of CMSs were shown in Fig. 3B and C, respectively. The CMSWs showed the strongest fluorescence intensity among the three CMSs, demonstrating the highest bio-retention ability. Furthermore, the bio-retention ability was highly correlated with morphologies in the order of CMSWs > CMSRs > CMSSs, and the bio-adhesion ratios were measured to be 77.26±0.06%, 65.22±0.08% and 47.65±0.05% at 5 min, respectively. CMSWs showed significantly stronger bio-adhesion ability on

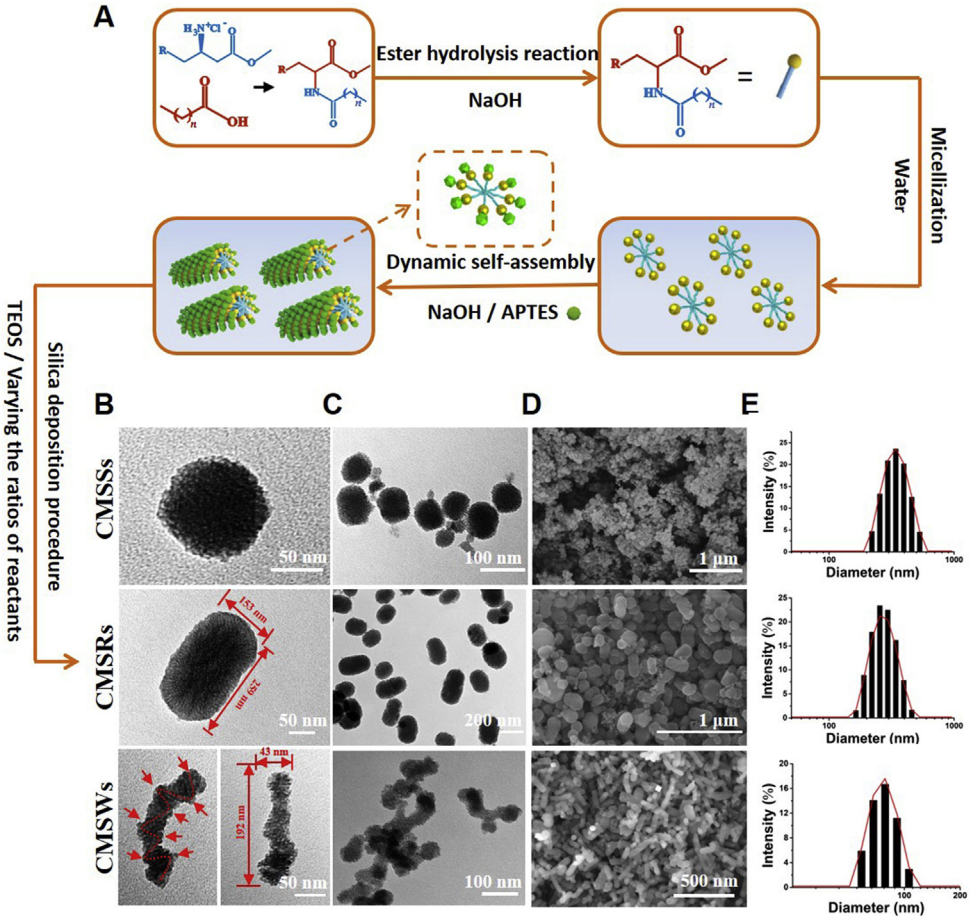

Figure 1 The formation mechanism (A), representative TEM images (B and C), representative SEM images of CMSs (D), and hydrodynamic diameters (E, based on the dynamic light scattering tests) of CMSs.

small intestinal mucosa because the three-dimension chiral topological structure increased the contact area ("surface" contact, Fig. 3A) and produced higher friction when coming into contact with the intestinal tract. It could then create more opportunities for the uptake of nanocarrier and increase the possibility for the passive absorption of the loaded therapeutic agents.

3.3. Mucus penetration of CMSs

Mucus is a viscoelastic biological hydrogel with a micrometer-ranged thickness and a nanometers-ranged pore size that protects the epithelial surface from penetration of most NPs[27,28]. We further explored the correlation between the morphologies of prepared CMSs and their penetration in mucus visualized using *ex vivo* image technology. Prior to the study, mucus was stained with RITC, and CMSs were labeled with FITC. After determining the fluorescence stability of FITC-CMSs (Supporting Information Fig. S3), the intestinal loops were ligated, incubated with FITC-CMSs, sectioned, and examined by CLSM instrument (Fig. 4B). The three-dimensional images disclosed that only a small proportion of red fluorescence was observed in CMSSs and CMSRs groups, while strong red fluorescence signal was found in CMSWs group. CMSWs showed a higher degree of mucus coverage than CMSSs and CMSRs, indicating the excellent mucoadhesion properties of CMSWs. Furthermore, the three-dimensional images disclosed that only a few particles in CMSSs and CMSRs groups were detected in the upper layer and without effectively migrating to the deep mucus layer. In contrast, CMSWs could penetrate deeper along the z-direction, presenting good permeability. It could conclude that CMSWs had superior mucus-penetrating than CMSSs and CMSRs[29]. The same results were also certificated by multiple-particle tracking technology, which could determine the particle moving trajectories in complex biological conditions. As was mapped in Fig. 4C, CMSSs and CMSRs moved within a narrow and limited area at 2 s and showed no obvious change in moving trajectories with the time increased to 10 s, indicating that the particles had weak diffusion ability and were nearly trapped by the mucus barrier. Compared to CMSSs and CMSRs, CMSWs showed dominant advantage toward mucus-penetration, which moved faster and freer in a large dimension and could continue to move in a random manner (in both horizontal and vertical) without being trapped. The results indicated that the Brownian motions of CMSWs were stronger though its particle size was even larger than CMSSs and CMSRs. Apart from the particle size, the particle shape also greatly influences the movement of NPs in the mucus layer. To be specific, spherical shape always meant a large section area, which was unbeneficial for the transport of NPs through the mucus layer with a tenacious mesh structure, and could easily be restricted and trapped by the viscoelastic mucins (Fig. 4A). On the contrary, CMSWs exhibited good penetration ability due to the small section area. What's more, from the mechanical perspective, the spherical CMSSs with highly symmetrical regular morphology could balance the bio-force from all directions, presenting small resultant forces and weak Brownian motions in the mucus layer,

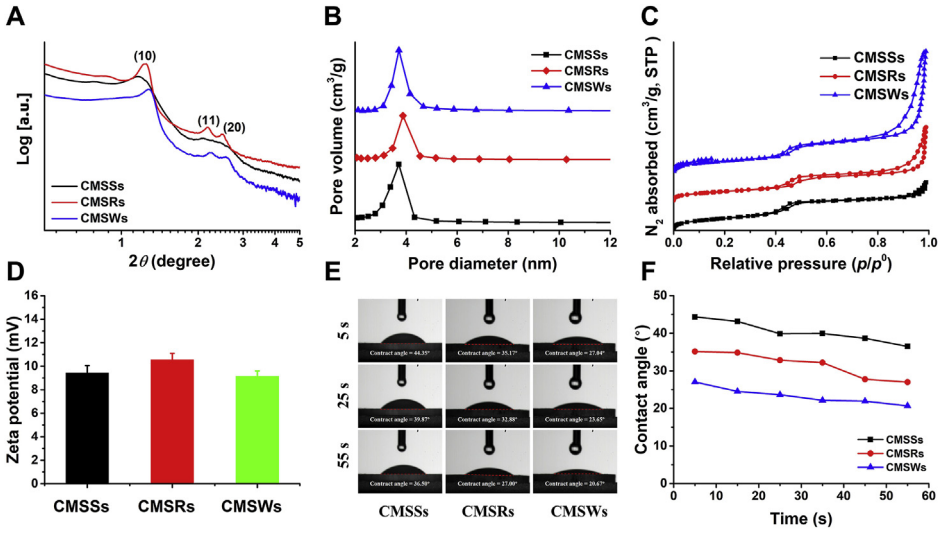

Figure 2 SAXS patterns (A), pore size distributions (B) and N_2 adsorption−desorption isotherms (C) of CMSs. (D) Zeta potential of CMSs. Data are presented as the mean ± SD of the mean (n = 3). (E) Contact angles of CMSs measured at the initial 5 s, the middle 25 s and the last 55 s. (F) The variation tendency of contact angles with time.

while the screw-like CMSWs with asymmetrical chiral topological structure could be driven by the uneven bio-force of microflows from all directions, resulting in strong resultant forces and free movements with good mucus-penetration ability (Fig. 4B). These results were also consistent with the pervious findings of Yu et al.[10], that rod-like NPs with large AR value were proved to penetrate the mucus layer easily through rotational dynamics. We believed that the "rotational motion" on the nanorods was also an evidence of the uneven bio-force of shear flow facilitated by the non-spherical structure. In this case, the "rotational motion" of CMSWs was further enhanced because the rotational torque was easier to produce on the irregular morphology, making it easier to produce rotational torque on the local irregular surface, and the movement could be amplified on the three-dimension chiral topological structure with regular slopes (functioned as screws). Thus, we could experimentally and theoretically conclude that CMSWs with small section area and irregular morphology exhibited stronger and flexible mucus penetration abilities.

3.4. *Cellular uptake of CMSs*

To explore the effect of morphology on the cellular uptake, Caco-2 cells were incubated with FITC-CMSs, and CLSM was applied to observe the fluorescence intensity originating from FITC-labeled CMSs. As can be seen from Fig. 5A, CMSSs exhibited the relative weak green fluorescence of FITC, and CMSWs displayed the strongest fluorescent signals among three engineered CMSs. The green fluorescence intensity in CMSSs, CMSRs and CMSWs groups increased in turn, indicating that the highest efficiency of cell entry occurred in CMSWs group. The large contact area ("surface" contact) and small section area facilitated the uptake of CMSWs. Meanwhile, the three-dimension chiral topological structure of CMSWs with regular slopes functioned as "screws" and made it hard to slip out while being uptake. These results could also be traced back to the fact that geometric topological structure of nanocarriers is closely associated with their functionality[30], which might attribute to specific endocytosis mechanisms. Thus, three specific inhibitors of cytochalasin D, chlorpromazine and Mβ-CD were introduced to identify cellular uptake pathways of CMSs. We could acquire the useful information from Fig. 5B and C that the cell entry efficiency of CMSSs was significantly influenced by chlorpromazine with a decrease in cellular uptake amount up to 50%, whereas the inhibition of Mβ-CD and cytochalasin D on the cellular internalization was less than 20%. This finding discovered that the cell uptake of CMSSs in Caco-2 cells was mainly depended on the clathrin-mediated endocytosis. For the rod-like CMSRs, a distinct reduction of the cellular uptake (approximately 50%) occurred after pre-incubation with chlorpromazine and Mβ-CD inhibitors, while the effect of cytochalasin D on cellular uptake could be negligible, suggesting that both clathrin-mediated and caveolae-mediated endocytosis were involved in the cellular internalization. Additionally, chlorpromazine had no effect on the cell entry efficiency of the screw-like CMSWs, but yet the influence of cytochalasin D and Mβ-CD inhibitors were more obvious than chlorpromazine, demonstrating that macropinocytosis and caveolae-mediated endocytosis were

Table 1 Specific surface area, pore volume, pore diameter and drug loading capacity of CMSs.

Sample	S_{BET} (m^2/g)	V_t (cm^3/g)	W_{BJH} (nm)	C_d (%)	AUC_{0-t} (μg/mL·h)
CMSSs	311	1.2	3.7	26.9 ± 2.4	4.67×10^5
CMSRs	221	1.2	3.7	18.5 ± 2.3	2.16×10^5
CMSWs	297	1.3	3.8	20.4 ± 1.6	1.22×10^6

CMSSs, chiral mesoporous silica nanospheres; CMSRs, chiral mesoporous silica nanorods; CMSWs, chiral mesoporous silica nano-screws; S_{BET}, specific surface area; V_t, pore volume; W_{BJH}, pore diameter; C_d, drug loading capacity; AUC_{0-t}, area under the curve. Data are expressed as mean ± SD (n = 3).

actively participated in the cellular uptake of CMSWs. Therefore, it could conclude that the endocytosis pathway of nonspherical NPs was more complex and always involved in two or multiple pathways[14]. Moreover, caveolae-mediated endocytosis was proved to have higher transport efficiency than that of clathrin-mediated endocytosis[31]. Because the vesicle coated with clathrin could be decomposed and did not remain stable under the acidic environment in the process of clathrin-dependent endocytosis, in which a fraction of internalized NPs might be recycled back to the plasma membrane where they gather around a new vesicle bud again[32]. Thus, the cellular uptake of CMSWs was more efficient than CMSSs and CMSRs. These studies revealed that the topological structure of NPs had strongly influence their abilities on overcoming both mucus and cellular barriers, which were crucial for determining the final destiny of nanocarriers in bio-systems.

3.5. *Retention of CMSs in the GI tract*

Considering the superiorities of CMSWs in bio-adhesion, mucus penetration and cellular uptake, it could be reasonably speculated that CMSWs would exhibit superior retention ability in the GI tract instead of being quickly washed out by the turnover of mucus. The FITC-CMSs were orally administered to fasted SD rats, the stomach and small intestine were excised, and the retention behavior of FITC-CMSs was studied visualized using *in vivo* fluorescence imaging analysis. As shown in Fig. 3E–G at 1 h post administration, a little fluorescence signal of CMSSs was captured in stomach, and a strong fluorescence signal was discovered in small intestinal. Then the fluorescence intensity in the stomach increased slightly at 2 h, but decreased rapidly at 4 h. Moreover, the fluorescence intensity in the small intestine started to decline with a rapid speed at 2 h and almost disappeared at 6 h. These results demonstrate that CMSSs showed fast gastrointestinal clearance with a short retention time due to the small contact area and the smooth surface resulted from the topological structure of nanosphere as aforementioned in the bio-adhesion part. Compared with CMSSs, CMSRs did not present detectable fluorescence signal in stomach and small intestine tissues at 1 h post administration. Then the fluorescence intensity in stomach and small intestine increased suddenly at 2 h, gradually decreased with the extension of administration time and almost disappeared after 12 h. As for CMSWs, obvious fluorescence signal was appeared in

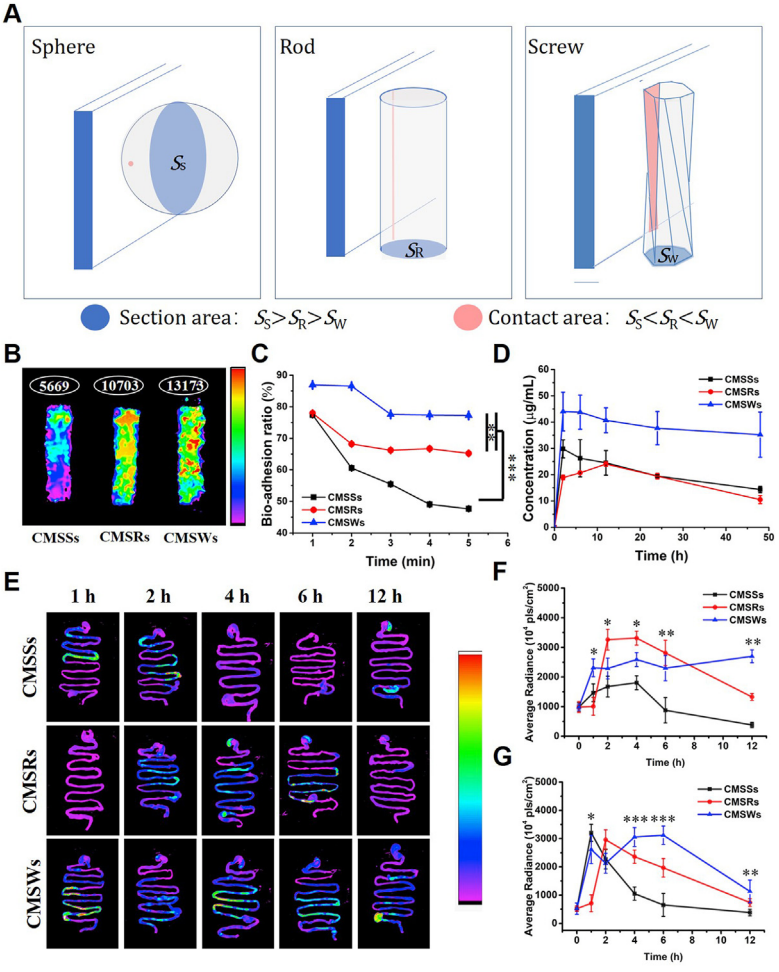

Figure 3 *In vivo* and *in vitro* bio-retention of CMSs with different morphologies. (A) The conceptual comparison in the sectional area and contact area of sphere, rod-shaped and screw-like structures. (B) Bio-retention images of CMSs on the mucus layer of small intestine (the white circles show the average fluorescence intensity of CMSs, indicating the bio-retention performance of CMSs). (C) Bio-retention profiles of CMSs on the mucus layer of small intestine. (D) Time-dependent plasma concentration of CMSs after oral administration. (E) Images of CMSs remained in the whole GI tract at different intervals after oral administration. (F and G) The average radiance of CMSs in stomach and small intestine at different times, respectively. Data are presented as the mean ± SD of the mean ($n = 3$). *$P < 0.05$, **$P < 0.01$, and ***$P < 0.001$.

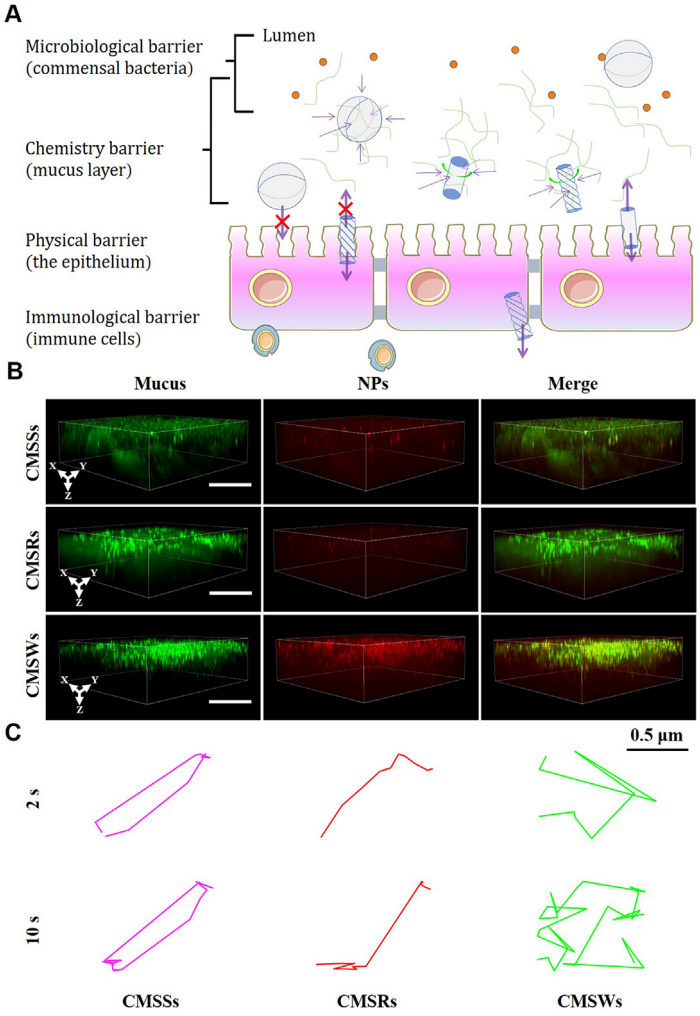

Figure 4 (A) Schematic illustration of CMSs with different topological structures in crossing IEB (mainly including the mucus layer and epithelial cells). (B) Three-dimensional images of mucoadhesion and mucus penetration. Green: mucus stained with RITC. Red: NPs. Scale bar = 50 μm. Depth: 70 μm. (C) The representative trajectories of CMSs in mucus solutions at 2 and 10 s.

stomach and small intestine tissues at 1 h after administration. With the increasing capture time, the fluorescence intensity of CMSWs in the small intestine was stronger than that of CMSSs and CMSRs, and the apparent fluorescence signal could still be captured at 12 h, indicating the strongest intestinal retention ability of CMSWs and providing great probability for the oral adsorption of nanocarriers.

3.6. Blood circulation of CMSs

On the basis of the results mentioned above, we concluded that CMSWs with ideal structure could effectively overcoming IEB *via* multiple topological mechanisms, and hold promise to achieve satisfactory oral absorption. To investigate the oral absorption process of CMSs, the *in vivo* blood circulation of CMSs was studied after oral administration. It was found that the blood circulation was quite different for CMSs (Fig. 3D). Generally speaking, nanocarrier should be designed to enter blood circulation rapidly and efficiently to exert a better therapeutic effect. As shown in Fig. 3D, compared to CMSSs and CMSRs, CMSWs showed superior oral absorption in both adsorption rate and adsorption amount. To be specific, 2 h after administration, CMSs began to show efficient distributions in blood. With the increase of administration time, the plasma concentration of CMSSs decreased significantly. For CMSRs, the maximum plasma concentration was reached at 12 h after administration, and the plasma concentration showed a decreasing trend with the extension of administration time to 48 h. It should be noticed that, although CMSRs exhibited superior retention ability than CMSSs in the GI tract, it still showed lower blood circulation, because of its larger particle size. Contrastingly, CMSWs still maintained a high plasma concentration even after 48 h, implying a longer blood circulation time, which might also increase the chance of drug absorption when it was served as a drug delivery platform. In a word, CMSWs achieved satisfactory absorption by exhibiting high-level plasma concentrations and longer sustained blood circulation, and the AUC of CMSWs was 2.61- and 5.65-times higher than that of CMSSs and CMSRs, respectively. It provided direct evidence that the topological structure of nanocarriers had great effect on their oral absorption process.

3.7. Drug loading and release behavior of DOX@CMSs

The above experiments demonstrated that screw-like CMSWs with ideal topological structure hold promise to be an efficient oral

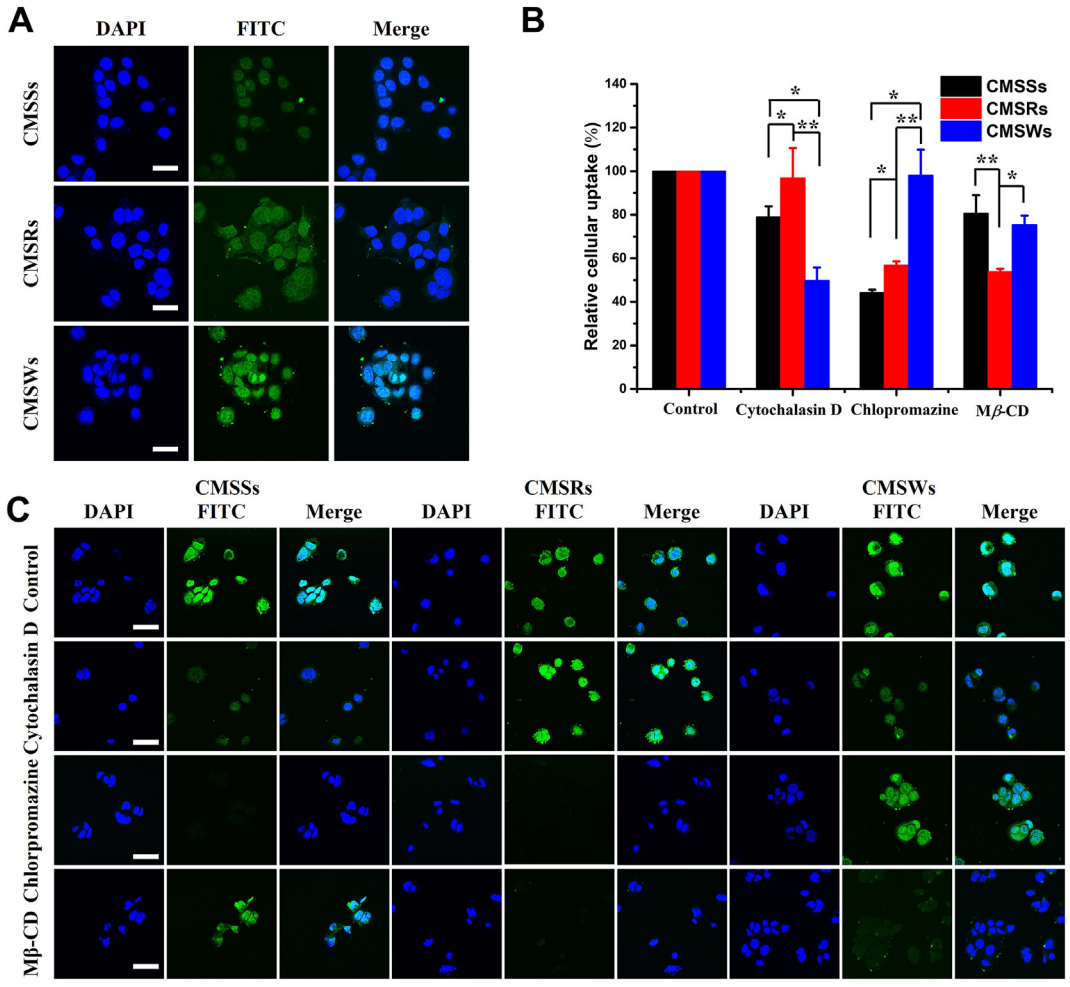

Figure 5 (A) CLSM images of Caco-2 cells after incubation with FITC-CMSs for 4 h. Scale bar = 50 μm. (B) Cellular uptake amounts of CMSs after incubation with specific inhibitors quantified by Image J software. (C) CLSM images of Caco-2 cells after incubation with FITC-CMSs in the presence of specific inhibitors: cytochalasin D, chlorpromazine and Mβ-CD. Scale bar = 30 μm. Data are presented as the mean ± SD of the mean (n = 3). *P < 0.05 and **P < 0.01.

drug delivery platform *via* multiple topological mechanisms. To further verify this point, DOX was served as the model drug and was effectively encapsulated into CMSs (confirmed by IR analysis, Supporting Information Fig. S4) by organic solvent drying method. The drug loading capacity of CMSSs, CMSRs and CMSWs were 26.9±2.4%, 18.5±2.3% and 20.4±1.6% (*w*/*w*), respectively. The results were positive correlated with the surface area (Table 1). As displayed in the XRD patterns (Fig. 6A), DOX was presented in crystalline state. Nevertheless, CMSs before and after drug loading exhibited broad bands in the range of 5°−45° (2θ), indicating the transformation of DOX crystalline state after loading into CMSs. Moreover, DSC analysis also confirmed the amorphous state of DOX after incorporating into nanocarriers (Supporting Information Fig. S5).

Before the drug release study, the wettability measurements of DOX@CMSs were conducted to provide some insights from the interfacial behavior. As displayed in Supporting Information Figs. S6A and B, after loading into CMWSs, the wettability of DOX was improved. Then the drug release of DOX@CMSs was determined by dialysis method in pH 7.4 PBS with DOX as a control (Fig. 6B). We found that DOX showed an initial burst release step with an extreme fast release at the initial 30 min, and the cumulative release amount of DOX reached up to 90% under normal physiological conditions (pH 7.4) after 3 h. After incorporating into CMSs, the release rate of DOX significantly reduced, and the cumulative release amount of DOX@CMSSs, DOX@CMSRs and DOX@CMSWs were 11%, 16% and 18% after 72 h, respectively. This sustainable release behavior of CMSs might be attributed to the limited mesoporous channels.

Furthermore, the potential of pH responsive drug delivery was also explored by selecting PBS medium with different pH values (pH 7.4, 6.5 and 5.0) to mimic the environment of normal tissues, tumor tissues and endosomes, respectively (Fig. 6C)[33]. At the first 24 h, DOX@CMSWs presented only 16% DOX release at pH 7.4 PBS, 20% DOX release at pH 6.5 PBS and 25% DOX release at pH 5.0 PBS, indicating a pH-dependent release manner. This phenomenon could be explained by the protonation of the amino groups on the inner and outer surfaces of CMSWs[34]. The DOX release continued to increase under pH 5.0 after 24 h, and the cumulative release amount reached up to 35% after 72 h. However, the release under pH 7.4 PBS and pH 6.5 PBS was complete after 36 h. From the above results, we could infer that CMSWs had the potential to delivery drugs in a controlled manner with the pH responsiveness.

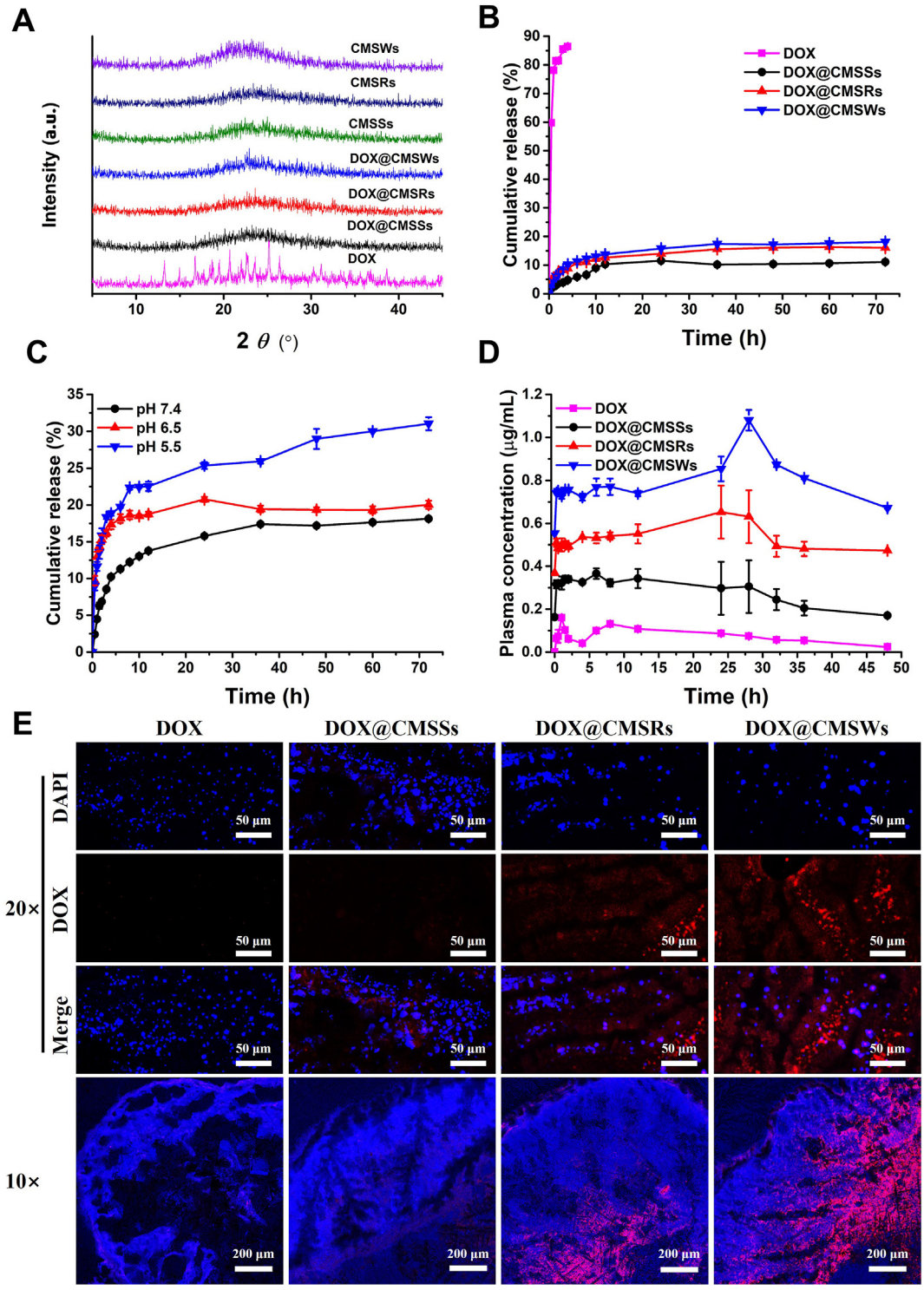

Figure 6 (A) XRD patterns of CMSs before and after DOX loading, indicating the successful drug loading. (B) *In vitro* release profiles of DOX and DOX@CMSs in pH 7.4 PBS. (C) *In vitro* release profiles of DOX@CMSWs in PBS medium with different pH values (pH 7.4, pH 6.5 and pH 5.0). (D) Plasma concentration *vs* time curves of DOX and DOX@CMSs in SD rats after oral administration. (E) CLSM images of DOX absorption at intestinal tissue acquired at 2 h after oral administration. Blue: nuclei of the intestinal villi stained with DAPI. Red: Dox.

3.8. Oral absorption of DOX@CMSs

To investigate the oral absorption process of DOX@CMSs, fasted SD rats were orally administered the FITC-CMSs, the middle small intestine tissues were collected, sliced using frozen section method and analyzed by CLSM. According to Fig. 6E, almost no red fluorescence signal of DOX was appeared in the DOX group. On the contrary, the fluorescence signal of DOX became stronger after being incorporated into CMSs, but the fluorescence intensity and the fluorescence distribution in each DOX@CMSs were quite

Table 2 Pharmacokinetic parameters obtained after oral administration of DOX and DOX@CMSs in SD rats.

Parameter	DOX	DOX@CMSSs	DOX@CMSRs	DOX@CMSWs
$AUC_{0-\infty}$ (mg/L·h)	4.00 ± 0.02	5.57 ± 1.63	11.03 ± 1.18	13.94 ± 0.56
$MRT_{0-\infty}$ (h)	24.58 ± 0.34	16.84 ± 2.36	34.28 ± 6.18	29.73 ± 0.66
$t_{1/2}$ (h)	12.62 ± 0.58	5.87 ± 2.19	16.60 ± 4.16	11.04 ± 0.48
T_{max} (h)	1.00	13.33 ± 12.70	24.00	28.00
C_{max} (mg/L)	0.16 ± 0.01	0.23 ± 0.04	0.29 ± 0.01	0.57 ± 0.04
F_{rel} (%)	100	139	276	348

Data are expressed as mean ± SD (n = 3). $AUC_{0-\infty}$, area under the curve; C_{max}, maximum concentration; F_{rel}, relative bioavailability; $MRT_{0-\infty}$, mean residence time; $t_{1/2}$, half-life; T_{max}, peak time.

different. To be specific, after loading into CMSSs and CMSRs, weak fluorescence signals of DOX were observed in the lumen. Especially, DOX@CMSSs group showed little fluorescence signal of DOX, while DOX@CMSRs exhibited stronger fluorescence signal. In particular, the fluorescence signal was greatly enhanced for DOX@CMSWs, and DOX was evenly distributed around the small intestine villi in DOX@CMSWs group, indicating that the penetration and absorption of DOX@CMSWs was more effective than that of DOX@CMSSs and DOX@CMSRs. Therefore, CMSWs could contact with intestinal epithelial cells evenly and enter into intestinal tissue effectively, while CMSSs and CMSRs rarely appeared in the regions of interest, which was consistent with the results of bio-retention (*in vitro*) and mucus penetration studies. In addition, DOX-CMSWs remained a stronger fluorescence signal in the GI tract instead of being rapidly washed away from the intestinal mucus even 12 h later, indicating a better retention property (Supporting Information Fig. S7).

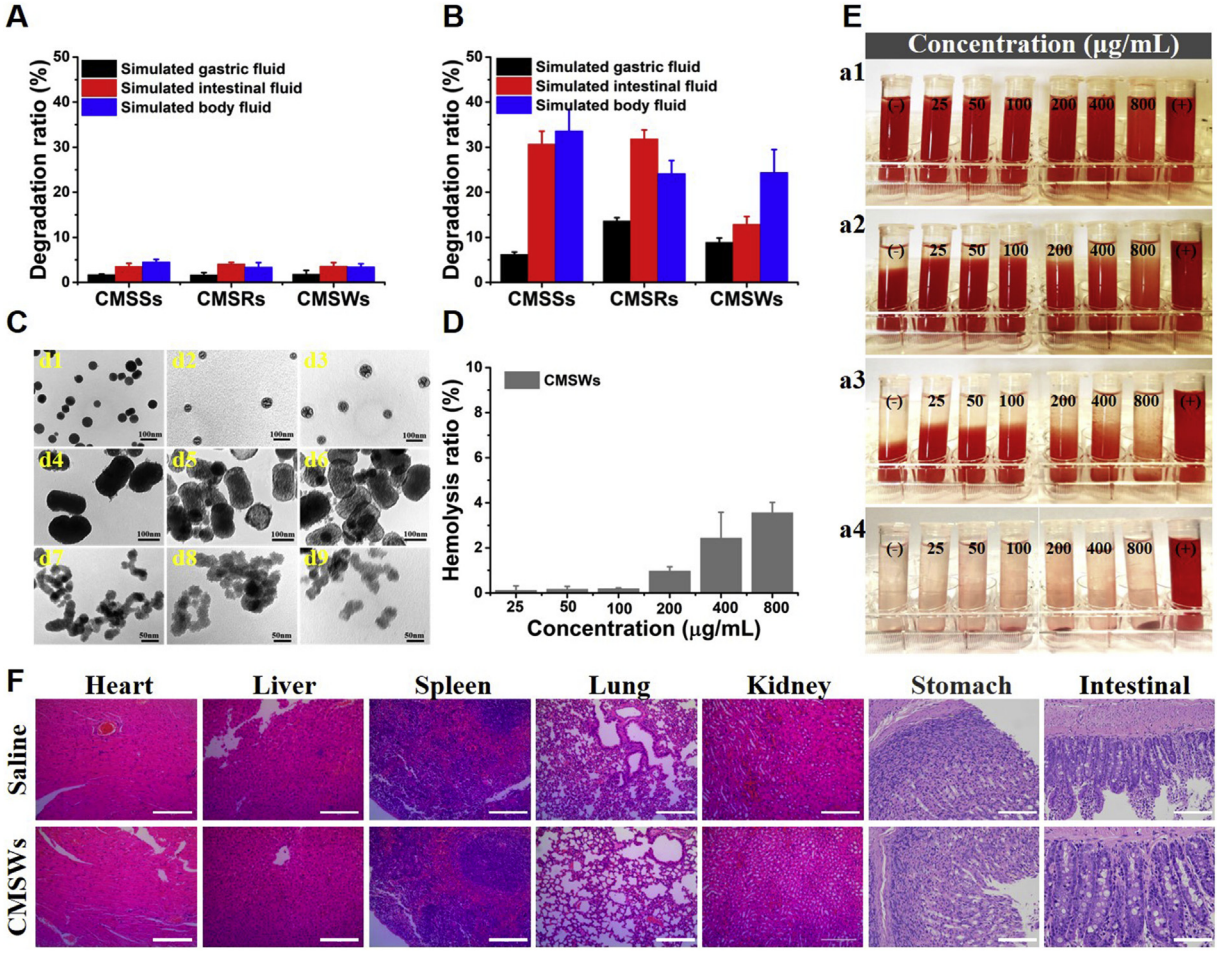

Figure 7 The calculated degradation rate of the CMSs after 48 h (A) and 1 week (B) of biodegradation. (C) TEM images of CMSs in SGF (d1, d4, d7), SIF (d2, d5, d8), and SBF (d3, d6, d9) after biodegradation for 1 week. (D) Hemolysis ratio of RBCs treated with CMSWs at different concentrations ranging from 25 to 800 μg/mL for 4 h. (E) Hemolytic photographs of RBCs incubated with different concentrations of CMSWs for 0.5 h (a1), 2 h (a2), 4 h (a3) and centrifugation after 4 h (a4) with D.I. water (+) and sterile normal saline (−) as positive and negative control, respectively. The presence of red hemoglobin in the supernatant indicates the damaged RBCs. (F) The H&E staining images of major tissues (heart, liver, spleen, lung and kidney) at the end of treatments of CMSWs. Data are represented as mean ± SD of the mean (n = 3). Scale bar = 200 nm.

These experiments demonstrated that CMSWs with ideal topological structure hold promise to be an efficient oral drug delivery platform. To further certificate the biological superiorities of CMSWs in oral drug absorption *in vivo*, pharmacokinetics studies of DOX and DOX@CMSs were carried out, the mean plasma concentration *versus* time curves were shown in Fig. 6D and the critical pharmacokinetic parameters were summarized in Table 2. For DOX, two peaks were observed in the profile at 1 and 8 h post-administration with the plasma concentration of 0.16 and 0.13 μg/mL, respectively. In comparison, only one peak was found in the profiles of DOX@CMSSs, DOX@CMSRs and DOX@CMSWs with C_{max} of 0.24, 0.29 and 0.57 μg/mL at the delayed T_{max} of 13, 24 and 28 h, respectively. It should be noted that after incorporating into CMSs with different morphologies, DOX showed the delayed T_{max} and $MRT_{0-\infty}$, which might be close related to the sustained drug release *in vivo*. More importantly, among DOX formulations, DOX@CMSWs achieved the highest C_{max}, which was approximately 3.56-, 2.38- and 1.97-fold higher than DOX, DOX@CMSSs and DOX@CMSRs, respectively. Similarly, the F_{rel} for DOX@CMSWs was approximately 3.48-, 2.50- and 1.26-fold higher than that of DOX, DOX@CMSSs and DOX@CMSRs, respectively. There is no doubt that CMSWs with ideal topological structures (*e.g.*, larger contact area, small section area and three-dimension chiral topological structure) showed the greatest potential in improving the oral delivery and enhancing the anticancer efficacy of DOX *via* topological mechanisms.

3.9. Degradability of CMSs

As drug delivery platforms, the degradability of CMSs was evaluated. In this study, the biodegradation of CMSs with different morphological property was studied in SGF, SIF and SBF mediums by weight loss (Fig. 7A and B) and TEM (Fig. 7C) methods. Firstly, after 48 h treatment, the weight loss of CMSs was much gentler (less than 5%) during the experiment period in all incubation mediums, confirming good stability while performing the delivery task. After 1 week treatment, CMSs showed low degradation ratio (<10%) in SGF, while presented faster degradation with higher degradation rate (>25%) in nearly neutral SIF and SBF. Compared to CMSSs and CMSRs, CMSWs showed a relatively slow degradation rate in SIF and SBF though it exhibited the best wettability. To further investigate the degradation mechanism, the degradation residues of CMSs (after 1 week treatment) were subject to TEM analysis, we could infer from Fig. 7C that the CMSs immersed in SGF did not show any obvious change in their morphology. However, significant morphological change was observed in SIF and SBF. It was worth noting that, for CMSSs, the degradation occurred around the pore channels, indicating the internal corrosion mechanism. In comparison, CMSRs and CMSWs were degraded from the external surfaces of particles. Herein, the external surfaces CMSRs and CMSWs guarded the internal pores, thus exhibiting slower degradation rates. These results suggested that CMSs showed good stability during the 48-h treatment period which protected the loaded cargoes from the harsh *in vivo* environment, and exhibited pH- and shape-dependent biodegradability in the long term with less safety concerns.

3.10. Biocompatibility assessment of CMSWs

Finally, the biocompatibility of CMSWs as nanocarrier was estimated both *in vitro* and *in vivo*. The blood compatibility of CMSWs was assessed by hemolysis assay at the concentration of 25−800 μg/mL. As shown in Fig. 7D and E, CMSWs does not show significant hemolytic activity and the hemolysis rate was lower than 5% even after incubation with high CMSWs concentration for 4 h, demonstrating good blood compatibility. The cell viability of CMSWs was evaluated on Caco-2 cells in the concentration range of 0−400 μg/mL by using MTT assay. As indicated in Supporting Information Fig. S8, the cell viability remains at a high level within the tested range. These results reveal that CMSWs didn't have toxicity, which provided prerequisite for the applications of CMSWs for biomedical applications.

Additionally, to detect the underlying toxicity of CMSWs for animals, the *in vivo* biosafety studies were carried out. No sudden death, unusual behaviors, and significant weight loss was observed during the 14-day experiments. The serum biomedical parameters and hematological parameters were analyzed (Supporting Information Figs. S9–S11). All these major parameters for the CMSWs treated animals were within the reference ranges and showed no substantial difference between the control groups. Moreover, the GI tract and the major tissues (heart, liver, spleen, lung and kidney) were excised for histological examination (Fig. 7F). The organ/body ratios (%) were all within the normal ranges (Supporting Information Table S1). H&E staining images revealed that CMSWs would not cause obvious histopathological abnormalities or damage after oral administration of CMSWs. Both the *in vitro* and *in vivo* experiments verified that CMSWs presented excellent biosafety and could be applied as a promising oral drug delivery platform.

4. Conclusions

In summary, the multiple topological advantages of CMSWs in overcoming IEB were listed as follows: (1) CMSWs with small section area exhibited good penetration ability; (2) the Brownian motion of CMSWs in mucus layer was promoted by the rotational torque produced on the irregular morphology and amplified by the screw-like shape with regular slopes; (3) CMSWs with the three-dimension chirality exhibited large contact area ("surface" contact) and strong bio-retention ability, which then facilitated the cellular uptake and prevented the slipping out. Compared to CMSSs and CMSRs, CMSWs possessed superior biological behaviors, including the strongest bio-adhesion, the best mucus-penetrating properties and the highest cellular uptake efficiency (contributed by the macropinocytosis and caveolae-mediated endocytosis pathways), which then resulted in longer intestinal retention time and superior adsorption in the blood circulation (up to 2.61- and 5.65-times in AUC). Meanwhile, CMSWs presented a controlled drug release behavior with pH responsiveness while serving as an oral delivery platform for DOX. As expect, it could efficiently promote the DOX absorption and penetration in the intestine, and finally improved the oral adsorption of DOX to a satisfactory level (up to 348%). Additionally, both the *in vitro* and *in vivo* experiments verified that excellent biodegradability and biocompatibility of CMSWs. We believe that, the successful attempt of CMSWs gives insights into the effect of the topological structures on the oral adsorption of nanocarriers and will provide useful information on the rational design of nano-DDS.

Acknowledgments

This article was funded by the National Natural Science Foundation of China (Nos. 81773672 and 81903550).

Author contributions

Sanming Li, Heran Li, and Yumei Wang designed and managed all the experiments, analyzed the data and wrote the manuscript. Jia Ke was responsible for the cellular experiments. Xianmou Guo and Kaijun Gou were involved in the design and implementation of animal experiments *in vivo*. Zhentao Sang, Yanbu Wang, and Yan Bian contributed materials and were involved in discussions of the data. All the authors critically reviewed and approved the manuscript.

Conflicts of interest

The authors declare no competing financial interest.

Appendix A. Supporting information

Supporting data to this article can be found online at https://doi.org/10.1016/j.apsb.2021.08.014.

References

1. Hristov D, McCartney F, Beirne J, Mahon E, Reid S, Bhattacharjee S, et al. Silica-coated nanoparticles with a core of zinc, L-arginine, and a peptide designed for oral delivery. *ACS Appl Mater Inter* 2020;**12**:1257−69.
2. Wu X, Qiu H, Che S. Controlling the pitch length of helical mesoporous silica (HMS). *Microporous Mesoporous Mater* 2009;**120**:294−303.
3. Jin H, Liu Z, Ohsuna T, Terasaki O, Inoue Y, Sakamoto K, et al. Control of morphology and helicity of chiral mesoporous silica. *Adv Mater* 2006;**18**:593−6.
4. Choonara BF, Choonara YE, Kumar P, Bijukumar D, du Toit LC, Pillay V. A review of advanced oral drug delivery technologies facilitating the protection and absorption of protein and peptide molecules. *Biotechnol Adv* 2014;**32**:1269−82.
5. Yun Y, Cho YW, Park K. Nanoparticles for oral delivery: targeted nanoparticles with peptidic ligands for oral protein delivery. *Adv Drug Deliv Rev* 2013;**65**:822−32.
6. Bao C, Liu B, Li B, Chai J, Zhang L, Jiao L, et al. Enhanced transport of shape and rigidity-tuned alpha-lactalbumin nanotubes across intestinal mucus and cellular barriers. *Nano Lett* 2020;**20**:1352−61.
7. Yu M, Yang Y, Zhu C, Guo S, Gan Y. Advances in the transepithelial transport of nanoparticles. *Drug Discov Today* 2016;**21**:1155−61.
8. Chen MC, Sonaje K, Chen KJ. A review of the prospects for polymeric nanoparticle platforms in oral insulin delivery. *Biomaterials* 2011;**32**:9826−38.
9. Lane LA, Qian X, Smith AM, Nie S. Physical chemistry of nanomedicine: understanding the complex behaviors of nanoparticles *in vivo*. *Annu Rev Phys Chem* 2015;**66**:521−47.
10. Yu M, Wang J, Yang Y, Zhu C, Su CH, Guo S, et al. Rotation-facilitated rapid transport of nanorods in mucosal tissues. *Nano Lett* 2016;**16**:7176−82.
11. Shiomi D. Erratum to: polar localization of MreB actin is inhibited by anionic phospholipids in the rod-shaped bacterium *Escherichia coli*. *Curr Genet* 2017;**63**:849.
12. Young KD. Bacterial morphology: why have different shapes?. *Curr Opin Microbiol* 2007;**10**:596−600.
13. Wang W, Wang P, Tang X, Elzatahry AA, Wang S, Al-Dahyan D, et al. Facile synthesis of uniform virus-like mesoporous silica nanoparticles for enhanced cellular internalization. *Acs Central Sci* 2017;**3**:839−46.
14. Zheng N, Li J, Xu C, Xu L, Li S, Xu L. Mesoporous silica nanorods for improved oral drug absorption. *Artif Cell Nanomed B* 2018;**46**:1132−40.
15. Maira AC, Mehdi J, Henry CF, Rama B. Helical and rod-shaped bacteria swim in helical trajectories with little additional propulsion from helical shape. *Sci Adv* 2016;**2**:e1601661.
16. Sycuro LK, Wyckoff TJ, Biboy J, Born P, Pincus Z, Vollmer W, et al. Multiple peptidoglycan modification networks modulate *Helicobacter pylori*'s cell shape, motility, and colonization potential. *PLoS Pathog* 2012;**8**:e1002603.
17. Frirdich E, Biboy J, Adams C, Lee J, Ellermeier J, Gielda LD, et al. Peptidoglycan-modifying enzyme Pgp 1 is required for helical cell shape and pathogenicity traits in *Campylobacter jejuni*. *PLoS Pathog* 2012;**8**:e1002602.
18. Wu SH, Mou CY, Lin HP. 3D cubic mesoporous silica microsphere as a carrier for poorly soluble drug carvedilol. *Chem Soc Rev* 2013;**42**:3862−75.
19. Hu B, Sun W, Li H, Sui H, Li S. Systematic modifications of amino acid-based organogelators for the investigation of structure−property correlations in drug delivery system. *Int J Pharm (Amst)* 2018;**547**:637−47.
20. Yokoi T, Yamataka Y, Ara Y, Sato S, Kubota Y, Tatsumi T. Synthesis of chiral mesoporous silica by using chiral anionic surfactants. *Microporous Mesoporous Mater* 2008;**103**:20−8.
21. Li J, Xu L, Yang B. Biomimetic synthesized chiral mesoporous silica: structures and controlled release functions as drug carrier. *Mat Sci Eng C-Mater* 2015;**55**:367−72.
22. Wang Y, Li W, Liu T, Xu L, Guo Y, Ke J, et al. Design and preparation of mesoporous silica carriers with chiral structures for drug release differentiation. *Mat Sci Eng C-Mater* 2019;**103**:109737.
23. Hu B, Wang J, Li J, Li S, Li H. Superiority of L-tartaric acid modified chiral mesoporous silica nanoparticle as a drug carrier: structure, wettability, degradation, bio-adhesion and biocompatibility. *Int J Nanomed* 2020;**15**:601−18.
24. De Haes W, Van Mol G, Merlin C, De Smedt SC, Vanham G, Rejman J. Internalization of mRNA lipoplexes by dendritic cells. *Mol Pharm* 2012;**9**:2942−9.
25. Sun J, Song Y, Lu M, Lin X, Liu Y, Zhou S, et al. Evaluation of the antitumor effect of dexamethasone palmitate and doxorubicin co-loaded liposomes modified with a sialic acid−octadecylamine conjugate. *Eur J Pharmaceut Sci* 2016;**93**:177−83.
26. Lin Y-S, Haynes CL. Synthesis and characterization of biocompatible and size-tunable multifunctional porous silica nanoparticles. *Chem Mater* 2009;**21**:3979−86.
27. Boegh M, Nielsen H. Mucus as a barrier to drug delivery-understanding and mimicking the barrier properties. *Basic Clin Pharmacol* 2015;**116**:179−86.
28. Anderski J, Mahlert L, Mulac D, Langer K. Mucus-penetrating nanoparticles: promising drug delivery systems for the photodynamic therapy of intestinal cancer. *Eur J Pharm Biopharm* 2018;**129**:1−9.
29. Yang X, He D, He X, Wang K, Tang J, Zou Z, et al. Synthesis of hollow mesoporous silica nanorods with controllable aspect ratios for intracellular triggered drug release in cancer cells. *ACS Appl Mater Inter* 2016;**8**:20558−69.
30. Kinnear C, Moore TL, Rodriguez-Lorenzo L, Rothen-Rutishauser B, Petri-Fink A. Form follows function: nanoparticle shape and its implications for nanomedicine. *Chem Rev* 2017;**117**:11476−521.
31. McMahon HT, Boucrot E. Molecular mechanism and physiological functions of clathrin-mediated endocytosis. *Nat Rev Mol Cell Biol* 2011;**12**:517−33.
32. Doherty GJ, McMahon HT. Mechanisms of endocytosis. *Annu Rev Biochem* 2009;**78**:857−902.
33. Zhao X, Wei Z, Zhao Z, Miao Y, Qiu Y, Yang W, et al. Design and development of graphene oxide nanoparticle/chitosan hybrids showing ph-sensitive surface charge-reversible ability for efficient intracellular doxorubicin delivery. *ACS Appl Mater Inter* 2018;**10**:6608−17.
34. Cui L, Liu W, Liu H, Qin Q, Wu S, He S, et al. pH-Triggered charge-reversal mesoporous silica nanoparticles stabilized by chitosan oligosaccharide/carboxymethyl chitosan hybrids for effective intracellular delivery of doxorubicin. *ACS Appl Bio Mater* 2019;**2**:1907−19.